공학석사 학위논문

Co-Fe Phosphide@Graphitic Carbon Nitride Nanosheet Modified Separator for High-Performance Lithium-Sulfur Batteries

고 성능 리튬-황 배터리를 위한 코발트-철 인화물 및 흑연 질화 탄소 나노시트를 이용한 분리막 표면 개질

2023년 2월

서울대학교 융합과학기술대학원

응용바이오공학 전공

유 태 현

Co-Fe Phosphide@Graphitic Carbon Nitride Nanosheet Modified Separator for High-Performance Lithium-Sulfur Batteries

지도 교수 박 원 철

이 논문을 공학석사 학위논문으로 제출함
2023년 1월

서울대학교 융합과학기술대학원
응용바이오공학 전공
유 태 현

유태현의 공학석사 학위논문을 인준함

2023년 1월

위 원 장 임 형 준 (인)

부위원장 박 원 철 (인)

위 원 김 정 민 (인)

Abstract

Co-Fe Phosphide@Graphitic Carbon Nitride Nanosheet Modified Separator for High-Performance Lithium-Sulfur Batteries

Taehyun Yoo

Department of Applied Bioengineering

Graduate School of Convergence Science and Technology

Seoul National University

Lithium-sulfur (Li-S) battery is a promising next-generation energy storage device due to its high theoretical capacity (1,675 mAh g^{-1}), environment-friendliness, low cost, and natural abundance. However, the shuttle effect and sluggish kinetics of lithium polysulfides (LiPs) hinder its commercialization. Herein, I report the synthesis of cobalt iron phosphide@graphitic carbon nitride nanosheet (CFP@CN) modified separator for Li-S batteries. The Li-S cell with CFP@CN separator (CFP@CN-PP) exhibits a high specific capacity of 786.4 mAh g^{-1} at 1C. Furthermore, the Li-S cell with CFP@CN-PP can still retain a

discharge capacity of 528.3 mAh g^{-1} and a capacity decay rate of only 0.084% per cycle after 650 cycles. And, the Li-S cell with CFP@CN-PP maintains high coulombic efficiency above 99% after 650 cycles. These results indicate that the CFP@CN with a large specific surface can alleviate the shuttle effect by strong chemical interaction with lithium polysulfides. Furthermore, thanks to high electrical conductivity of CFP@CN, the utilization of sulfur and redox kinetics can be improved. This study offers useful insights into designing materials for modified separator of lithium-sulfur battery.

Keywords: lithium-sulfur battery; separator; two-dimension; cobalt iron phosphide; graphitic carbon nitride

Student Number: 2021-27069

Contents

List of Figures

1. Introduction

1.1. Lithium-Sulfur batteries

Recently, with the rapid development of electric vehicles and portable electronic devices, demand for next-generation secondary batteries with high energy density is greatly increasing. A commercial lithium-ion battery (LIB) is composed of a cathode, including a transition metal oxide or a transition metal phosphate, and an anode as graphite, which has excellent cycle characteristics. However, LIB displays low practical energy density, making it difficult to meet the aforementioned demand [1], [2]. On the other hand, lithium-sulfur (Li-S) battery is a promising next-generation energy storage devices, owing to its high theoretical capacity (1,675 mAh g^{-1}), environment-friendliness, low cost, and natural abundance compared to commercial lithium-ion battery [3], [4], [5], [6], [7]. However, despite these advantages, Li-S battery is difficult to commercialize due to several problems [8], [9]: 1) Low utilization of sulfur due to low conductivity of sulfur and lithium sulfide (Li_2S). 2) A volume change (~80%) occurs during charging and discharging due to the density difference between sulfur and Li_2S. 3) A shuttle effect of lithium polysulfides occurs during charge and discharge process. Due to the shuttle effect, lithium polysulfides (LiPs) dissolve into the electrolyte and move to the surface of the lithium metal anode, and then form lithium sulfide, which causes a loss of active

materials and severe capacity fading. Due to these problems, the obtained capacity and energy density of Li-S are very low. To solve these problems, recent studies on cathode structure design [10], [11], [12], modification of separator [13], [14], [15], and introduction of all-solid electrolyte [16], [17] have been conducted. Among the various strategies, a general strategy is to solve the above-mentioned problems through cathode structure design. The cathode structure design significantly can improve the capacity and cycle performance of the Li-S battery, but it is inevitable to add inactive materials in the host material and inject more electrolytes for high sulfur loading, reducing the energy density. In addition, the complex synthesis process of cathode is very uneconomical [18], [19]. Therefore, many researchers have recently focused on developing modified separator.

1.2. Modified separator in Lithium-Sulfur batteries

The modified separator physically and chemically suppresses the shuttle effect of polysulfides and acts as an upper current collector. Early modified separator studies were mainly conducted using carbon materials [20], [21]. Thanks to excellent conductivity of carbon materials, sulfur utilization can be increased. Nevertheless, due to non-polar property of carbon, the shuttle effect can only be suppressed physically, resulting in a serious capacity decay in long-

term cycle performance. In order to solve this problem, recent studies have been conducted to suppress the shuttle effect through strong chemical adsorption with LiPs through heteroatom doping in carbon materials [22], [23]. In addition, transition metal compounds such as transition metal oxides (TMO) and transition metal nitrides (TMN) have been found to strongly suppress the shuttle effect through Lewis acid-base interactions [24], [25], [26]. Among them, thanks to high conductivity and significant electrical catalyst performance than other transition metal compounds, transition metal phosphide (TMP) has been studied recently [27], [28]. Also, TMPs are promising candidates for electrochemical applications because of their ease of synthesis.

Graphitic carbon nitride (g-C_3N_4) has a graphite-like layered structure and consists of continuous tri-s-triazine units [29]. Thanks to high contents of pyridinic N in its structure, g-C_3N_4 can have strong chemical adsorption with LiPs, improve electrochemical performance and suppress the shuttle effect [30]. In addition, due to polymeric nature of g-C_3N_4, it has excellent structural flexibility and can mitigate volume expansion. Nevertheless, due to low conductivity of g-C_3N_4, the utilization of sulfur participating in electrochemical reaction is low [31]. Therefore, g-C_3N_4 is usually doped for conductivity or used with conductive materials.

1.3. Objective

In this work, I synthesized cobalt-iron phosphide@graphitic carbon nitride nanosheet (CFP@CN) by electrostatic self-assembly method. The obtained CFP@CN has some benefits for Li-S battery. First, restacking occurs within CFP structure due to van der Waals forces. This reduces the surface area and decreases ionic conductivity [32]. However, heterostructure of CFP@CN made of different two 2D materials solves these problems [33], [34]. Thus, thanks to heterostructure, there are many active sites for LiPs capturing and many pathways for lithium-ion transport. Second, Co and Fe have strong catalytic abilities, which can boost redox kinetics of LiPs [35]. Third, CFP has good electrical conductivity, which promotes redox reaction kinetics and increases sulfur utilization [27], [36]. Finally, Co, Fe, P, and N in CFP@CN can alleviate the shuttle effect through strong chemisorption with LiPs. With these advantages, the Li-S battery containing CFP@CN coated separator displays a high capacity of 786.4 mAh g^{-1} at 1C and a low capacity decay rate of 0.08 % per cycle after 650 cycles at 1C. Therefore, the CFP@CN separator improved the electrochemical performance of Li-S battery.

2. Experimental Section

2.1 Materials

All chemicals and reagents were used as received without further purification. Cobalt chloride hexahydrate ($CoCl_2 \cdot 6H_2O$, 99.0%), and tris(hydroxymethyl)aminomethane (Tris-NH_2, 99.0%) were purchased from Samchun Chemicals. Iron chloride tetrahydrate ($FeCl_2 \cdot 4H_2O$, 99.0%) was purchased from Sigma-Aldrich. Sodium hypophosphite ($NaH_2PO_2 \cdot H_2O$, 97.0%) was purchased from Junsei. Urea (NH_2CONH_2, 99.0%~100.5%) was purchased from Alfa Aesar

2.2 Preparation of graphitic carbon nitride (g-C_3N_4) nanosheet

15 g of urea was put in a crucible with a cover and then heated for 4 h in a muffle furnace at 550 °C for 4 h. Subsequently, the obtained pale yellow sample was collected after cooling to room temperature and ground into powder. The grounded sample was further heated at 500 °C for 2 h in an open crucible. Finally, the g-C_3N_4 nanosheet was obtained.

2.3 Synthesis of Co-Fe Tris-NH_2 (CFT)

Initially, $CoCl_2 \cdot 6H_2O$ (1.427 g) and $FeCl_2 \cdot 4H_2O$ (0.795 g) were dissolved in 100 mL of deionized water to prepare Solution A and Tris-NH_2 (12.11 g) was

dissolved in the same amount of deionized water to prepare Solution B. After that solution A and solution B were mixed and placed in an oven at 80 °C for 20 h. The obtained gelled product was washed with deionized water for 3 times and freeze-dried for 3 days.

2.4 Preparation of Co-Fe Tris-NH_2@g-C_3N_4 nanosheet (CFT@CN)

The CFT (0.05 g) and g-C_3N_4 (0.05 g) were dissolved in 20 mL of deionized water, respectively. Then, the CFT solution was sonicated for 30 minutes and then slowly mixed with the g-C_3N_4 solution. The mixed solution was then freeze-dried for 3 days. Finally, the obtained product was collected and labeled as CFT@CN.

2.5 Preparation of Co-Fe phosphide@g-C_3N_4 nanosheet (CFP@CN)

The CFT@CN (0.1 g) and NaH_2PO_2 (2 g) were put in two crucibles respectively. The two crucibles were placed in a tube furnace together and then heated at 350 °C for 3 h with a heating rate of 2 °C per min under Ar atmosphere. Finally, the resultant product was collected after cooling to room temperature and labeled as CFP@CN nanosheet.

2.6 Preparation of modified separator

To prepare modified separator, the CFP@CN (9 mg) was mixed with polyvinylidene fluoride (PVdF) (1 mg) and then dispersed in 10 mL NMP. After ultra-sonic treatment, the dispersed solution is poured into a polypropylene (PP) separator, and a modified separator is made using vacuum filtration. The modified separator was dried in a vacuum oven at 50 °C for 4 h.

2.7 Preparation of Li_2S_6 solution

For the visualized adsorption tests, the sulfur and Li_2S with a molar ratio of 5:1 were dissolved in a mixture solvent of 1,3-dioxolane (DOL)/1,2-dimethoxyethane (DME) with a volume ratio of 1:1 under vigorous stirring at 60 °C for 24 h in the glove box.

2.8 Material characterization

Field emission scanning electron microscope (FE-SEM; Hitachi S-4800, 15 kV) was used to obtain scanning electron microscopy (SEM) images. The morphologies and elemental distributions of the samples were characterized by energy-filtering transmission electron microscopy (EFTEM) and energy-dispersive X-ray spectroscopy (EDS, LIBRA 120). X-ray photoelectron spectroscopy (XPS) was performed using AXIS-HIS (Kratos Analytical) with Mg/Kα X-ray source. The nitrogen adsorption-desorption tests were performed

using a BELSORP-mini II (MicrotracBEL). The crystallographic structures were characterized using an X-ray diffractometer (Bruker New D8 Advance) with Cu Kα radiation. Thermogravimetric analysis (TGA) was conducted using TGA/DSC 1 analyzer (Mettler Toledo) with a heating rate of 10 °C min^{-1} in N_2 atmosphere. Zeta potential tests were performed using a ZEN1020 (Malvern Instruments).

2.9 Electrochemical measurements

The sulfur/ketjen black (S/KB) electrode was synthesized by mixing sulfur, ketjen black, and 5 wt.% polyvinylidene fluoride (PVdF) in N-methyl-2-pyrrolidinone (NMP) with a mass ratio of 6:3:1. After mixing, the slurry casts onto carbon-coated Al foil and dried in vacuum oven at 50 °C to remove the solvent. The electrodes were cut to a diameter of 12 mm and the loading mass of sulfur was about 1 mg cm^{-2}. For the electrochemical test, the CR 2016 coin-type cell was assembled with S/KB electrode, Li metal, and separator. The electrolyte was mixed with a bis(trifluoromethane)sulfonimide lithium salt (1.0M) dissolved in a mixed solvent having a volume ratio of DOL/DME of 1:1, and a 1 wt.% $LiNO_3$ additive, and then 30 μL mg^{-1} was used for test. The CR-2016 cell was assembled in the argon-filled glovebox. The Galvanostatic charge-discharge tests were conducted using WBCS3000S cycler (WonATech

Co.) in a voltage range between 1.7 ~ 2.8 V vs. Li/Li^+ at different scan rates. Electrochemical impedance spectroscopy (EIS) was performed using a Zive SP1 (Zive Lab, WonATech Co).

2.10 Symmetric cells for cyclic voltammetry (CV) analysis

In order to prepare electrodes for symmetrical cells, CFP@CN and PVdF binder were mixed in NMP solvent to produce CFP@CN electrodes at a weight ratio of 9:1 The CFP electrode was manufactured in the same way. The symmetric cell was assembled by using two identical electrodes as the cathode and anode with polypropylene (PP) separator. As the electrolyte, 30μL mg^{-1} electrolyte containing 1.0 M LiTFSI and 0.4 M Li_2S_6 in a mixture of DOL/DME at a volume ratio of 1:1 was used. The cell assembled in the argon-filled glovebox. The symmetric cells were conducted in a potential range from −1.0 to 1.0 V vs. Li/Li^+.

3. Results and Discussion

Figure 1 schematically illustrates the synthesis process of Co-Fe phosphide@graphitic carbon nitride nanosheet (CFP@CN). First, a certain ratio of Co and Fe precursors were dissolved in deionized water, mixed slowly with the Tris-NH_2 solution, and stirred for 30 minutes. Then, the obtained dark brown solution was reacted at 80 °C for 20 hours. After that, the reactants were washed several times and freeze-dried to obtain CFT nanosheet. The g-C_3N_4 (CN) nanosheet was synthesized via two-step pyrolysis of urea [37]. The structure and morphology of samples were studied by scanning electron microscopy (SEM). As shown in **Figures 2a** and **b**, the SEM images of CFT and CN show a 2D structure. The CFT and CN were dissolved in deionized water, respectively, and the two solutions were slowly mixed. During the mixing process, the difference in surface charge between CFT and CN easily leads to self-assembly by electrostatic interactions. Finally, the CFP@CN nanosheet was synthesized by phosphorization of CFT@CN at 350 °C for 3 h.

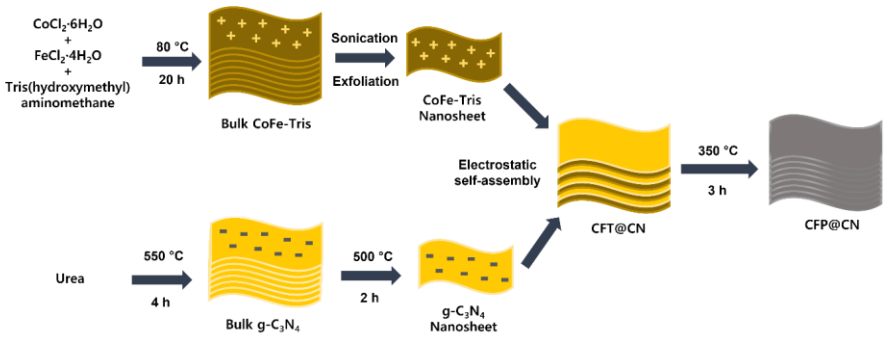

Figure 1. The schematic illustration of the synthesis of CFP@CN.

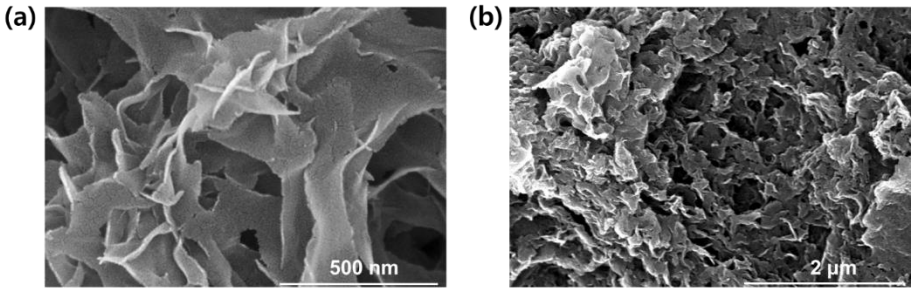

Figure 2. SEM images of (a) CFT and (b) CN.

As shown in **Figure 3a**, through the zeta potential test, the surface charge of CFT and CN has a positive charge and a negative charge, respectively.

The crystal structural characteristics of CN, CFT, CFT@CN, and CFP@CN were studied by X-ray diffraction (XRD) patterns. As displayed in **Figure 3b**, the strong peak at 27.4° corresponds to the interlayer stacking (002) of g-C_3N_4 [38]. The XRD pattern of CFT exhibits no obvious diffraction peaks, indicating the amorphous nature of the sample [39]. Besides, after mixing g-C_3N_4 and CFT, there is no significant change in the XRD patterns of CFT@CN, which indicates that there are no changes in structure during the self-assembly process. For XRD patterns of CFP@CN, the peak intensity of (002) decreased, which means that the crystallinity of CN decreased during the phosphorization process [40]. Also, as shown in **Figure 4**, the CoP and FeP are clearly formed after phosphorization of CFT@CN.

The morphology of CFP@CN and CFT@CN were examined using transmission electron microscopy (TEM). As shown in **Figure 3c**, the CFP and CN are stacked well without aggregation. Also, the TEM image shows a thin layer of CFP@CN. This structure increases the Li^+ diffusion and provides many active sites for chemical absorption with LiPs. Elemental mapping images of CFP@CN are shown in **Figure 3d** to confirm the elemental distribution of Co, Fe, P, N, C, and O in CFP@CN. Due to the inevitable oxidation of the surface

of CFP@CN, the element O is detected. The EDS mapping indicates that Co, Fe, P, and N are homogeneous distributions in CFP@CN, which can strongly interact with LiPs. As shown in **Figure 5**, The CFT@CN is also well stacked, indicating that electrostatic self-assembly between positive-charged CFT and negative-charged CN occurs well.

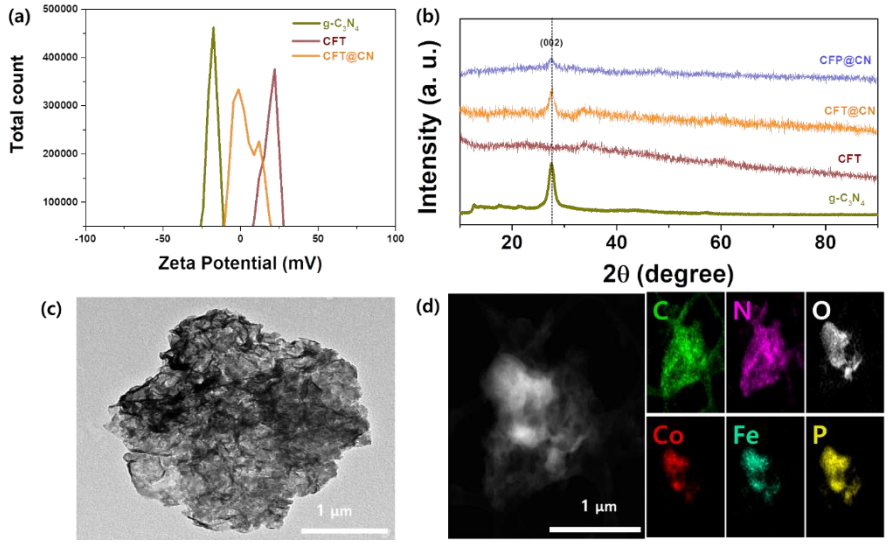

Figure 3. (a) Zeta potentials of g-C_3N_4, CFT, and CFT@CN in aqueous solution. (b) XRD patterns of g-C_3N_4, CFT, CFT@CN, and CFP@CN. (c) TEM image of CFP@CN. (d) Elemental mapping images of C, N, O, Co, Fe, and P of CFP@CN.

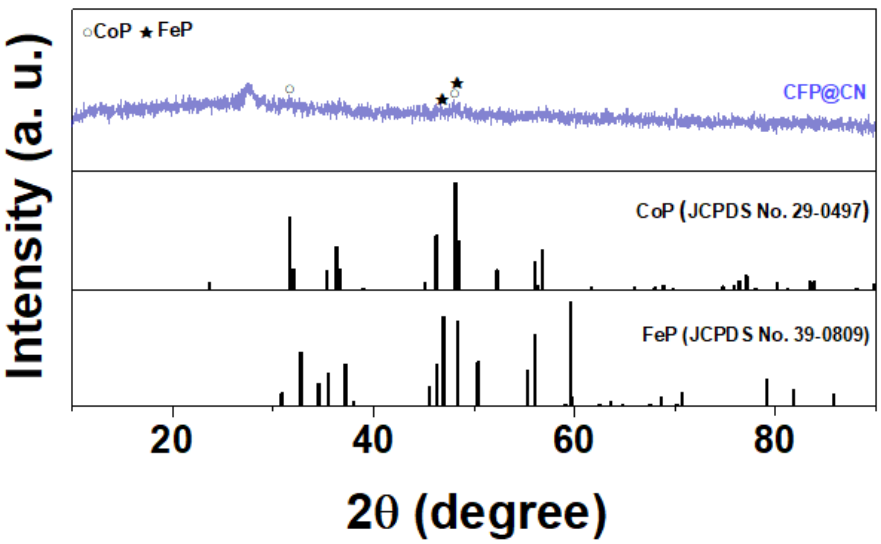

Figure 4. XRD pattern of CFP@CN.

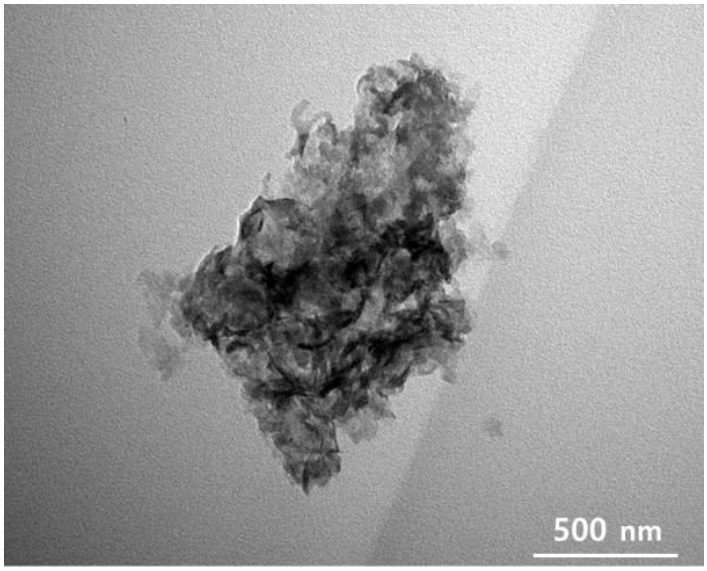

Figure 5. TEM image of CFT@CN.

The nitrogen adsorption-desorption tests were conducted in **Figure 6a.** The corresponding Brunauer-Emmett-Teller (BET) surface areas are 19.753 $m^2 g^{-1}$ and 1.5378 $m^2 g^{-1}$ for CFP@CN and CFP, respectively. This result indicates that due to the nature of the two-dimensional material, restacking within the CFP is caused by van der Waals forces. Fortunately, these problems are solved by heterostructure of CFP@CN constructed of different 2D materials. The addition of CN prevents restacking of CFP. Thus, thanks to this heterostructure, the CFP@CN nanosheet not only provides more active sites for chemical absorption with LiPs but also increase ionic conductivity. To investigate adsorption capability of CFP@CN toward LiPs, the visualized adsorption tests were conducted by adding 20mg CFP@CN and CN into the 4 mM Li_2S_6 solution, respectively. As shown in Inset of **Figure 6b**, the Li_2S_6 solution containing CFP@CN changes from yellow to almost transparent after 24h, while the Li_2S_6 solution containing CFP became pale yellow. The UV- Vis spectra of those supernatants after 24h were characterized in **Figure 6b**. The absorbance peak of Li_2S_6 is strong in the range of 250-350 nm. However, the peak of Li_2S_6 almost disappears after adding the CFP@CN. These results indicate that due to Co, Fe, P, and N present in CFP@CN, CFP@CN has strong LiPs adsorption ability which can interact with LiPs through polar-polar interaction and has a large specific surface area for LiPs capturing due to the

heterostructure.

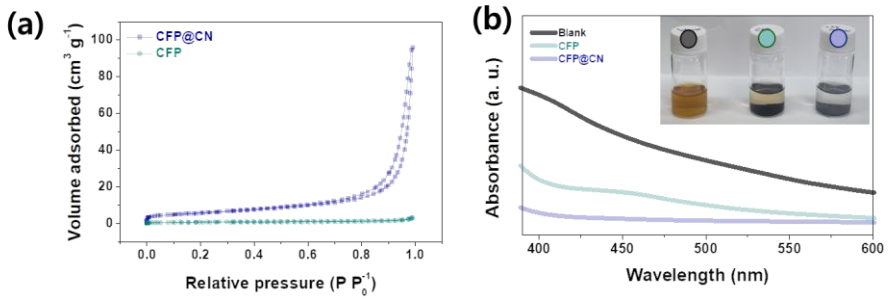

Figure 6. (a) N_2 adsorption/desorption isotherms of CFP@CN and CFP. (b) UV spectra and digital photographs of the Li_2S_6 solutions after addition of CFP@CN and CFP for 24 h.

To further study the chemical interaction between CFP@CN and LiPs, X-ray photoelectron spectroscopy (XPS) analysis was conducted before and after Li_2S_6 adsorption. The Co 2p high-resolution spectra of CFP@CN before and after adsorption of LiPs are shown in **Figure 7a.** Before absorption, the two deconvoluted peaks of Co 2p3/2 at 779.8 eV and Co 2p1/2 at 795.55 eV consist of Co−P bonding which verifies the successful formation of cobalt phosphide during the phosphorization process [41], [42]. Also, another two peaks of Co 2p3/2 at 783.36 eV and Co 2p1/2 at 799.22 eV are ascribed to Co−O bonding, indicating the inevitable surface oxidation of CFP@CN in air atmosphere [43]. After CFP@CN interacted with LiPs, the Co-P peaks are shifted to higher binding energy and the peak intensity ratio between Co-P/S and Co-O increases. These results confirm that the formation of the Co-S bond is due to the interaction between S atoms in LiPs and Co atoms in CFP@CN [44], [45]. In the Fe 2p spectrum shown in **Figure 7b**, the two peaks at 709.4 eV and 721.71 eV consist of Fe-P, Fe 2p3/2, Fe 2p1/2, respectively [46]. Another two peaks of Fe 2p3/2 at 713.02 eV and Fe 2p1/2 at 725.31 eV are ascribed to Fe−O bonding [47]. After interacting with LiPs, the intensity of Fe-O components decreases, and Fe-P peaks are moved to higher binding energy, which are corresponding with the formation of Fe-S bonds owing to the interaction between S atoms in LiPs and Fe atoms in CFP@CN [45]. Meanwhile, the N 1s and P 2p high-

resolution spectrum in **Figures 7c** and **d** show after interaction with LiPs. In the case of N 1s, all peaks shift could be observed and an additional N-Li band is formed during the adsorption process [45]. These results showed that N atom in CFP@CN can capture LiPs through strong chemical interaction and alleviate the shuttle effect. Similarly, a band shift could be observed in the P 2p spectrum due to electron transfer from P atom in CFP@CN to LiPs [48].

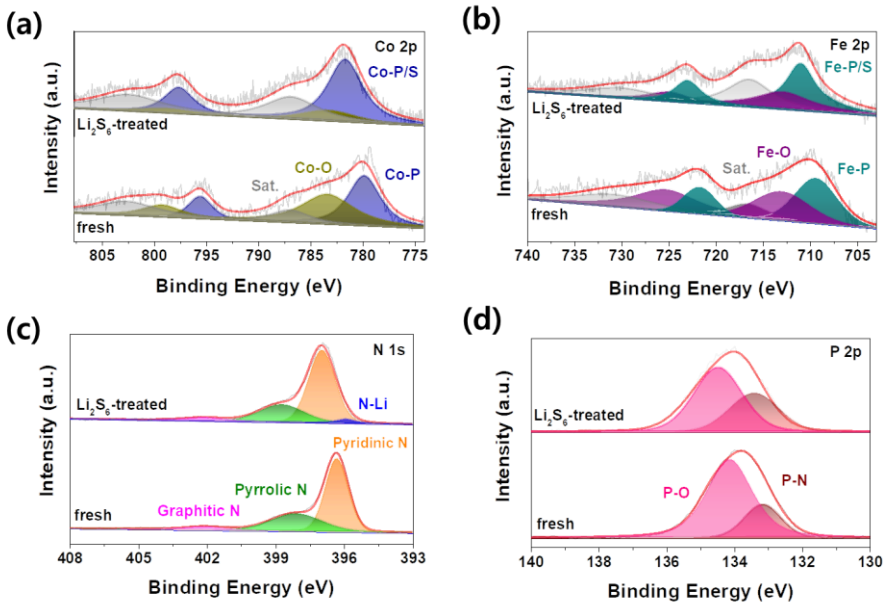

Figure 7. High-resolution XPS spectra of a) Co 2p, b) Fe 2p, c) N 1s, and d) P 2p before and after CFP@CN interaction with Li_2S_6.

In order to perform electrochemical tests, a cathode containing sulfur, ketjen black, and PVDF cast on carbon-coated Al foil as a current collector. The sulfur content and sulfur loading cathodes were 66 wt.% and about 1 mg cm^{-2}, respectively. The sulfur content was confirmed by using TGA as shown in **Figure 8**. A commercial polypropylene separator is named Bare PP. In addition, a polypropylene separator with CFP@CN coating and CFP coating is named CFP@CN-PP and CFP-PP, respectively. As shown in **Figure 9a**, the thickness of the CFP@CN separator is approximately 14 μm. Furthermore, as shown in **Figure 9b-d**, the CFP@CN-PP shows great affinity with the electrolyte than others. Compared to other separators, the contact angle of CFP@CN-PP is almost 0°. This result indicates that the CFP@CN-PP has good wettability, which can boost Li^+ transportation.

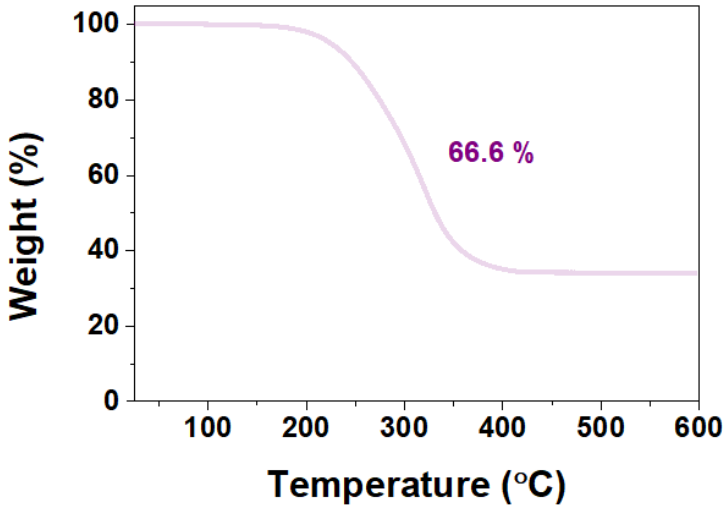

Figure 8. TGA curve of S/KB.

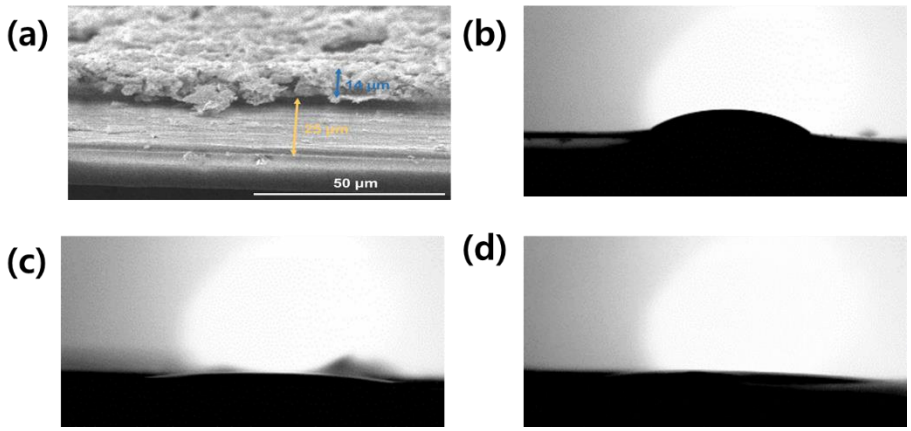

Figure 9. (a) Cross-sectional SEM image of CFP@CN-PP. Contact angle tests of (b) Bare PP, (c) CFP-PP, and (d) CFP@CN-PP.

To elucidate the electrocatalytic effect on conversion of LiPs, cyclic voltammetry (CV) tests of Li_2S_6 symmetric cells using CFP@CN or CFP electrodes as the working and counter electrodes were conducted at -1 to 1 V vs. Li/Li^+. As shown in **Figure 10a**, the CFP@CN electrode exhibits two pairs of distinct reduction and oxidation peaks. In contrast, only one redox peak was observed with the CFP electrode. Also, compared with the CFP electrode, the CFP@CN electrode shows a sharper peak shape and higher peak current. These results suggested that the CFP@CN nanosheet has strong catalytic ability and accelerates the reaction kinetics of LiPs conversion.

Electrochemical impedance spectroscopy (EIS) was conducted to further study the redox kinetics. In general, the semicircle at the high-frequency region is associated to charge transfer resistance (R_{ct}) and the inclined line at the low-frequency region is associated with diffusion of lithium ions [49]. As shown in **Figures 10b** and **c**, both the EIS results before and after cycling indicate that the R_{ct} of the cell with CFP@CN-PP is lower than that with CFP-PP and Bare PP. These results indicate that the CFP@CN-PP enhances ionic and electronic conductivity and boosts the transfer of electrons. Also, after cycling, the new semi-circle is related to the resistance by the solid electrolyte interphase (SEI) layer and the decrease in the R_{ct} value of all samples is due to the electrochemical activation during the cycle. In addition, as sulfur, the active

material, is redistributed during the cycle, the contact with the cathode increases, resulting in a lower R_{ct} value.

Furthermore, to estimate the Li^+ diffusion coefficient, CV measurements for CFP@CN-PP, CFP-PP, and Bare PP at different scan rates from 0.1 mV s^{-1} to 0.8 mV s^{-1} were conducted. The CV results of CFP@CN-PP and CFP-PP are shown in **Figures 10d** and **e**, respectively. The Li^+ diffusion coefficient was calculated by using the Randles-Sevcik equation below [50], [51]:

$$I_p = (2.69 \times 10^5) n^{1.5} A D_{Li}^{0.5} C_{Li} v^{0.5}$$

Herein I_p is the peak current, n represents the number of electrons that participate in the reaction, A represents the electrode area, D_{Li} represents the Li-ion diffusion coefficient, C_{Li} represents the concentration of Li^+ ions, and ν represents the scan rate. The D_{Li} values of the samples are calculated using the linear relationship between peak current and the square root of scan rates. In **Figures 10f** and **g**, the slopes of the fit of two peaks in the cell with CFP@CN-PP are higher than those in the cell with CFP-PP. These results indicate that the Li^+ diffusion is promoted due to the heterostructure of CFP@CN during the redox reaction, which enables high rate performance at high C rates.

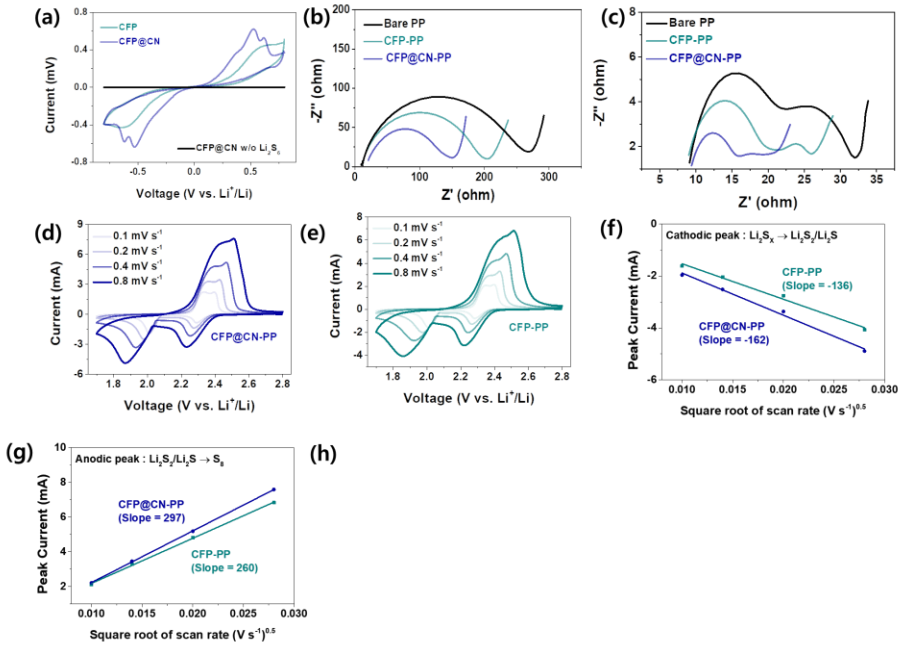

Figure 10. (a) CV curves of the different symmetric cells. Electrochemical impedance spectroscopy (EIS) data of the CFP@CN-PP, CFP-PP, and Bare PP cell (b) before and (c) after 100 cycles. (d,e) CV curves of CFP@CN-PP and CFP-PP cell at different scan rates from 0.1 to 0.8 mV s^{-1}, respectively. (f) Cathodic ($Li_2S_x \rightarrow Li_2S_2/Li_2S$) and (g) anodic peak current ($Li_2S_2/Li_2S \rightarrow Li_2S_8$) against the square root of scan rate for CFP@CN-PP and CFP-PP cell.

The rate performance was conducted at different current densities from 0.2 to 3C as illustrated in **Figure 11a**. The CFP@CN-PP cell exhibits average capacity of 986.4, 852.1, 786.4, 708, and 609.1 mAh g^{-1} at 0.2 C, 0.5 C, 1 C, 2 C, and 3 C, respectively. In contrast, the Li-S with CFP-PP and Bare PP exhibit much lower average capacity of 906, 741.5, 642.2, 550.3, 468.7 mAh g^{-1} and 880, 735.3, 576.5, 367.7, 174.5 mAh g^{-1} at 0.2 C, 0.5 C, 1 C, 2 C, and 3 C, respectively. At 3 C rate, the discharge capacity of the CFP-PP cell gradually decreases, but CFP@CN-PP cell shows constant discharge capacity, which has electrochemical stability even at high C rate. When the current density backed to 0.2 C, The CFP@CN-PP cell recovers well. These results indicate that thanks to heterostructure of CFP@CN, the CFP@CN-PP can accelerate fast Li^+ transportation and suppress the LiPs migration toward Li metal via chemical interaction. Furthermore, the long-term cycle performance of different modified separators was measured at 1 C. As shown in **Figure 11b**, the CFP@CN-PP exhibits an initial discharge capacity of 840 mAh g^{-1}, while the CFP-PP and Bare PP display discharge capacities of 622.1 and 104 mAh g^{-1}, respectively. In the case of the Li-S cell with Bare PP, the discharge capacity gradually increases up to about 40 cycles. This is because activation proceeds slowly due to poor wettability characteristic of Bare PP. After 650 cycles, the CFP@CN-PP can still retain capacity of 528.3 mAh g^{-1} and the capacity decay rate of only 0.084% per cycle. In contrast, the CFP-PP and Bare PP exhibit relatively low capacities of 271.7 and 96.1 mAh g^{-1} and the capacity fading rate

of 0.11% and 0.13% per cycle, respectively. These results indicated that the CFP@CN nanosheet with large specific surface not only alleviates LiPs migration with physical and chemical interaction but also boosts redox reaction which enhances sulfur utilization.

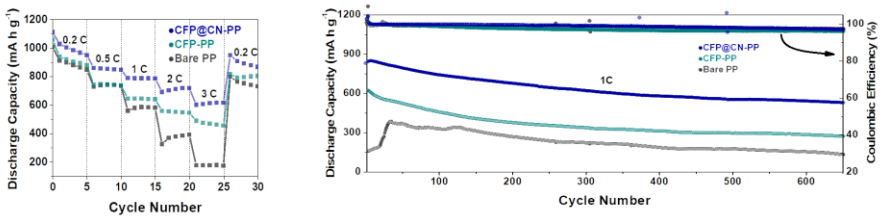

Figure 11. (a) Rate performances of CFP@CN-PP, CFP-PP, and Bare PP cell at different scan rates. (b) Cycling performances of CFP@CN-PP, CFP-PP, and Bare PP cell for 650 cycles at 1C.

4. Conclusions

In summary, the Co-Fe phosphide@g-C_3N_4 nanosheet (CFP@CN) was synthesized by electrostatic self-assembly. Then, the CFP@CN modified separator (CFP@CN-PP) was prepared by vacuum filtration. The obtained CFP@CN has large surface area, which can interact with LiPs through strong chemical absorption. Thanks to heterostructure of CFP@CN, there are many pathways for lithium-ion transport, resulting in increasing ionic conductivity. Also, transition metals such as Co and Fe in CFP@CN can improve the redox kinetics of LiPs. Furthermore, the CFP@CN can alleviate the shuttle effect of LiPs by the formation of N-Li bonds with CN and polar-polar interactions with CFP. Based on these benefits, the Li-S cell with CFP@CN separator shows a high discharge capacity of 786.4 mAh g^{-1} at 1 C. Also, after 650 cycles, the Li-S cell with CFP@CN separator can still exhibits a discharge capacity of 528.3 mAh g^{-1} and a capacity decay rate of only 0.084 % per cycle. This research offers useful information on selecting materials for modified separator of Li-S battery.

References

[1] M. Armand, J.-M. Tarascon, Building better batteries, Nature, 451 (2008) 652-657.

[2] B. Scrosati, J. Garche, Lithium batteries: Status, prospects and future, J. Power Sources, 195 (2010) 2419-2430.

[3] M. Arumugam, Y. z. Fu, S.-H. Chung, CX Zu and YS Su, Rechargeable Lithium–Sulfur Batteries, Chem. Rev, 114 (2014) 11751-11787.

[4] Q. Wu, X. Zhou, J. Xu, F. Cao, C. Li, Adenine derivative host with interlaced 2d structure and dual lithiophilic–sulfiphilic sites to enable high-loading Li–S batteries, ACS Nano, 13 (2019) 9520-9532.

[5] X. Ji, K.T. Lee, L.F. Nazar, A highly ordered nanostructured carbon–sulphur cathode for lithium–sulphur batteries, Nat. Mater., 8 (2009) 500-506.

[6] J. Balach, T. Jaumann, M. Klose, S. Oswald, J. Eckert, L. Giebeler, Functional mesoporous carbon-coated separator for long-life, high-energy lithium–sulfur batteries, Adv. Funct. Mater., 25 (2015) 5285-5291.

[7] P. Bruce, S. Freunberger, L. Hardwick, J. Tarascon, High energy storage Li-O_2 and Li-S batteries, Nat. Mater., 11 (2011) 19-29.

[8] M. Wild, L. O'Neill, T. Zhang, R. Purkayastha, G. Minton, M. Marinescu, G. Offer, Lithium sulfur batteries, a mechanistic review, Energy Environ. Sci., 2015, 8, 3477.

[9] H. Yao, G. Zheng, P.-C. Hsu, D. Kong, J.J. Cha, W. Li, Z.W. Seh, M.T. McDowell, K. Yan, Z. Liang, Improving lithium–sulphur batteries through spatial control of sulphur species deposition on a hybrid electrode surface, Nat. Commun., 5 (2014) 3943.

[10] C. Hu, H. Chen, Y. Shen, D. Lu, Y. Zhao, A.-H. Lu, X. Wu, W. Lu, L. Chen, In situ wrapping of the cathode material in lithium-sulfur batteries, Nat. Commun., 8 (2017) 479.

[11] S. Evers, L.F. Nazar, New approaches for high energy density lithium–sulfur battery cathodes, Acc. Chem. Res., 46 (2013) 1135-1143.

[12] H. Wang, Y. Yang, Y. Liang, J.T. Robinson, Y. Li, A. Jackson, Y. Cui, H. Dai, Graphene-wrapped sulfur particles as a rechargeable lithium–sulfur battery cathode material with high capacity and cycling stability, Nano Lett., 11 (2011) 2644-2647.

[13] D. Gueon, J.T. Hwang, S.B. Yang, E. Cho, K. Sohn, D.-K. Yang, J.H. Moon, Spherical macroporous carbon nanotube particles with ultrahigh sulfur loading

for lithium–sulfur battery cathodes, ACS Nano, 12 (2018) 226-233.

[14] S. Bai, X. Liu, K. Zhu, S. Wu, H. Zhou, Metal–organic framework-based separator for lithium–sulfur batteries, Nat. Energy, 1 (2016) 16094.

[15] Z.A. Ghazi, X. He, A.M. Khattak, N.A. Khan, B. Liang, A. Iqbal, J. Wang, H. Sin, L. Li, Z. Tang, MoS_2/celgard separator as efficient polysulfide barrier for long-life lithium–sulfur batteries, Adv. Mater., 29 (2017) 1606817.

[16] T. Lei, W. Chen, W. Lv, J. Huang, J. Zhu, J. Chu, C. Yan, C. Wu, Y. Yan, W. He, Inhibiting polysulfide shuttling with a graphene composite separator for highly robust lithium-sulfur batteries, Joule, 2 (2018) 2091-2104.

[17] C. Wang, Y. Li, Y. Zhang, L. Zhang, C. Gu, X. Wang, J. Tu, Integrating a 3D porous carbon fiber network containing cobalt with artificial solid electrolyte interphase to consummate advanced electrodes for lithium–sulfur batteries, Mater. Today Energy, 24 (2022) 100930.

[18] Y. Zhang, Y. Wu, Y. Liu, J. Feng, Flexible and freestanding heterostructures based on COF-derived N-doped porous carbon and two-dimensional MXene for all-solid-state lithium-sulfur batteries, Chem. Eng. J., 428 (2022) 131040.

[19] Y. Ren, Q. Zhai, B. Wang, L. Hu, Y. Ma, Y. Dai, S. Tang, X. Meng, Synergistic Adsorption-Electrocatalysis of 2D/2D heterostructure toward high

performance Li-S batteries, Chem. Eng. J., 439 (2022) 135535.

[20] Z. Gao, Z. Xue, Y. Miao, B. Chen, J. Xu, H. Shi, T. Tang, X. Zhao, TiO_2@ Porous carbon nanotubes modified separator as polysulfide barrier for lithium-sulfur batteries, J. Alloy. Compd., (2022) 164249.

[21] Z. Zhang, Y. Lai, Z. Zhang, J. Li, A functional carbon layer-coated separator for high performance lithium sulfur batteries, Solid State Ion., 278 (2015) 166-171.

[22] J. Zhu, Y. Ge, D. Kim, Y. Lu, C. Chen, M. Jiang, X. Zhang, A novel separator coated by carbon for achieving exceptional high performance lithium-sulfur batteries, Nano Energy, 20 (2016) 176-184.

[23] X. Song, S. Wang, G. Chen, T. Gao, Y. Bao, L.-X. Ding, H. Wang, Fe-N-doped carbon nanofiber and graphene modified separator for lithium-sulfur batteries, Chem. Eng. J., 333 (2018) 564-571.

[24] Q. Li, Y. Liu, L. Yang, Y. Wang, Y. Liu, Y. Chen, X. Guo, Z. Wu, B. Zhong, N, O co-doped chlorella-based biomass carbon modified separator for lithium-sulfur battery with high capacity and long cycle performance, J. Colloid Interface Sci., 585 (2021) 43-50.

[25] X. Wang, L. Yang, Y. Wang, Q. Li, C. Chen, B. Zhong, Y. Chen, X. Guo,

Z. Wu, Y. Liu, Novel functional separator with self-assembled MnO_2 layer via a simple and fast method in lithium-sulfur battery, J. Colloid Interface Sci., 606 (2022) 666-676.

[26] K. Xu, X. Liang, L.-L. Wang, Y. Wang, J.-F. Yun, Y. Sun, H.-F. Xiang, Tri-functionalized polypropylene separator by rGO/MoO_2 composite for high-performance lithium–sulfur batteries, Rare Met., 40 (2021) 2810-2818.

[27] H. Zhang, R. Dai, S. Zhu, L. Zhou, Q. Xu, Y. Min, Bimetallic nitride modified separator constructs internal electric field for high-performance lithium-sulfur battery, Chem. Eng. J., 429 (2022) 132454.

[28] Z. Pu, T. Liu, I.S. Amiinu, R. Cheng, P. Wang, C. Zhang, P. Ji, W. Hu, J. Liu, S. Mu, Transition-metal phosphides: activity origin, energy-related electrocatalysis applications, and synthetic strategies, Adv. Funct. Mater., 30 (2020) 2004009.

[29] Y. Ren, B. Wang, H. Liu, H. Wu, H. Bian, Y. Ma, H. Lu, S. Tang, X. Meng, CoP nanocages intercalated MXene nanosheets as a bifunctional mediator for suppressing polysulfide shuttling and dendritic growth in lithium-sulfur batteries, Chem. Eng. J., 450 (2022) 138046.

[30] Z. Meng, Y. Xie, T. Cai, Z. Sun, K. Jiang, W.-Q. Han, Graphene-like g-

C_3N_4 nanosheets/sulfur as cathode for lithium–sulfur battery, Electrochim. Acta, 210 (2016) 829-836.

[31] J. Wang, Z. Meng, W. Yang, X. Yan, R. Guo, W.-Q. Han, Facile synthesis of rGO/ g-C_3N_4/CNT microspheres via an ethanol-assisted spray-drying method for high-performance lithium–sulfur batteries, ACS Appl. Mater. Interfaces, 11 (2018) 819-827.

[32] J. Wang, V. Malgras, Y. Sugahara, Y. Yamauchi, Electrochemical energy storage performance of 2D nanoarchitectured hybrid materials, Nat. Commun., 12 (2021) 3563.

[33] Y. Xue, Q. Zhang, W. Wang, H. Cao, Q. Yang, L. Fu, Opening two-dimensional materials for energy conversion and storage: a concept, Adv. Energy Mater., 7 (2017) 1602684.

[34] C. Wang, N. Sakai, Y. Ebina, T. Kikuchi, M.R. Snowdon, D. Tang, R. Ma, T. Sasaki, Three-in-one cathode host based on Nb 3 O 8/graphene superlattice heterostructures for high-performance Li–S batteries, J. Mater. Chem. A, 9 (2021) 9952-9960.

[35] M. Wang, Q. Liang, J. Han, Y. Tao, D. Liu, C. Zhang, W. Lv, Q.-H. Yang, Catalyzing polysulfide conversion by g-C_3N_4 in a graphene network for long-

life lithium-sulfur batteries, Nano Res., 11 (2018) 3480-3489.

[36] D. Liu, C. Zhang, G. Zhou, W. Lv, G. Ling, L. Zhi, Q.H. Yang, Catalytic effects in lithium–sulfur batteries: promoted sulfur transformation and reduced shuttle effect, Adv. Sci., 5 (2018) 1700270.

[37] Y. Zhang, T. Mori, J. Ye, M. Antonietti, Phosphorus-doped carbon nitride solid: enhanced electrical conductivity and photocurrent generation, J. Am. Chem. Soc., 132 (2010) 6294-6295.

[38] H. Gao, H. Yang, J. Xu, S. Zhang, J. Li, Strongly coupled g-C_3N_4 nanosheets-Co_3O_4 quantum dots as 2D/0D heterostructure composite for peroxymonosulfate activation, Small, 14 (2018) 1801353.

[39] S. Yang, Y. Gong, J. Zhang, L. Zhan, L. Ma, Z. Fang, R. Vajtai, X. Wang, P.M. Ajayan, Exfoliated graphitic carbon nitride nanosheets as efficient catalysts for hydrogen evolution under visible light, Adv. Mater., 25 (2013) 2452-2456.

[40] D. Kim, S. Park, B. Yan, H. Hong, Y. Cho, J. Kang, X. Qin, T. Yoo, Y. Piao, Synthesis of Remarkably Thin Co–Fe Phosphide/Carbon Nanosheet for Enhanced Oxygen Evolution Reaction Electrocatalysis Driven by Readily Generated Active Oxyhydroxide, ACS Appl. Energy Mater., 5 (2022) 2400-

2411.

[41] Q. Lin, Z. Li, T. Lin, B. Li, X. Liao, H. Yu, C. Yu, Controlled preparation of P-doped g-C_3N_4 nanosheets for efficient photocatalytic hydrogen production, Chin. J. Chem. Eng., 28 (2020) 2677-2688.

[42] X. Chen, X. Ding, C. Wang, Z. Feng, L. Xu, X. Gao, Y. Zhai, D. Wang, A multi-shelled CoP nanosphere modified separator for highly efficient Li–S batteries, Nanoscale, 10 (2018) 13694-13701.

[43] Z. Ye, Y. Jiang, J. Qian, W. Li, T. Feng, L. Li, F. Wu, R. Chen, Exceptional adsorption and catalysis effects of hollow polyhedra/carbon nanotube confined CoP nanoparticles superstructures for enhanced lithium–sulfur batteries, Nano Energy, 64 (2019) 103965.

[44] Y. Zhong, L. Yin, P. He, W. Liu, Z. Wu, H. Wang, Surface chemistry in cobalt phosphide-stabilized lithium–sulfur batteries, J. Am. Chem. Soc., 140 (2018) 1455-1459.

[45] Y. Chen, W. Zhang, D. Zhou, H. Tian, D. Su, C. Wang, D. Stockdale, F. Kang, B. Li, G. Wang, Co–Fe mixed metal phosphide nanocubes with highly interconnected-pore architecture as an efficient polysulfide mediator for lithium–sulfur batteries, ACS Nano, 13 (2019) 4731-4741.

[46] C. Zhang, R. Du, J.J. Biendicho, M. Yi, K. Xiao, D. Yang, T. Zhang, X. Wang, J. Arbiol, J. Llorca, Tubular CoFeP@ CN as a Mott–Schottky catalyst with multiple adsorption sites for robust lithium− sulfur batteries, Adv. Energy Mater., 11 (2021) 2100432.

[47] G. Xia, Z. Zheng, J. Ye, X. Li, M.J. Biggs, C. Hu, Carbon microspheres with embedded FeP nanoparticles as a cathode electrocatalyst in Li-S batteries, Chem. Eng. J., 406 (2021) 126823.

[48] X. Zhao, Z. Zhang, X. Cao, J. Hu, X. Wu, A.Y.R. Ng, G.-P. Lu, Z. Chen, Elucidating the sources of activity and stability of FeP electrocatalyst for hydrogen evolution reactions in acidic and alkaline media, Appl. Catal. B Environ., 260 (2020), 118156-118163.

[49] X. Wang, H. Liu, Q. Wang, G. Zhang, C. Pei, H. Wang, S. Guo, In-situ fabrication of dense structure nitrogen-doped carbon nanotube embedded Co/Co_2P accelerating the electrochemical kinetics of lithium-sulfur battery, Appl. Surf. Sci., 595 (2022) 153488.

[50] L. Peng, Z. Wei, C. Wan, J. Li, Z. Chen, D. Zhu, D. Baumann, H. Liu, C.S. Allen, X. Xu, A fundamental look at electrocatalytic sulfur reduction reaction, Nat. Catal., 3 (2020) 762-770.

[51] X. Tao, J. Wang, C. Liu, H. Wang, H. Yao, G. Zheng, Z.W. Seh, Q. Cai, W. Li, G. Zhou, Balancing surface adsorption and diffusion of lithium-polysulfides on nonconductive oxides for lithium–sulfur battery design, Nat. Commun., 7 (2016) 11203.

국 문 초 록

리튬-황 배터리는 높은 이론 용량, 친환경성, 저비용 및 자연상의 풍부함으로 인해 주목받고 있는 차세대 에너지 저장장치이다. 그러나 리튬 폴리설파이드의 셔틀효과 및 느린 산화, 환원반응으로 인해 리튬-황 배터리의 상용화에 어려움이 있다. 이 연구에서, 코발트-철 인화물 및 흑연 질화 탄소 나노시트를 정전기적 인력을 통해 합성했다. 이를 리튬-황 배터리의 분리막 표면 개질 물질로써 사용하여 적용해본 결과 전류 밀도 1 C 에서 786.4 mAh g^{-1}의 방전용량을 보였다. 또한 전류 밀도를 1 C 로 인가하여 650회의 충•방전을 진행했을 때 여전히 528.3 mAh g^{-1}의 방전용량과 충•방전 1회 당 0.084 %의 용량 감소율을 보였다. 이러한 결과는 큰 비표면적을 갖는 코발트-철 인화물 및 흑연 질화 탄소 나노시트가 리튬 폴리설파이드와의 강력한 화학적 상호작용에 의해 셔틀 효과를 완화할 수 있음을 나타낸다. 또한 코발트-철 인화물 및 흑연 질화 탄소 나노 시트의 높은 전기전도도 덕분에 반응에 참여하는 황의 사용량을 증가시키고 산화, 환원 반응을 향상시킬 수 있었다. 본 연구는 리튬-황 배터리의 분리막 표면 개질을 위한 물질을 설계하는 데 유용한 정보를 제공한다.

주요어: 리튬-황 배터리, 분리막, 2차원, 코발트-철 인화물, 흑연 질화 탄소

학 번: 2021-27069